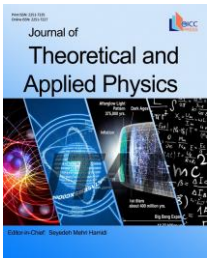

Volume 19, Issue 6, 192560 (1-18)

Journal of Theoretical and Applied Physics (JTAP)

https://doi.org/10.57647/j.jtap.2025.1906.60

The Role of Physical Quantities on the Quantum Dot and Quantum Well Spin-polarized Lasers in Steady and Dynamical States

Abuzar Shakeri*, S.Avaz Zadeh

Department of Physics, Shi.C., Islamic Azad University, Shiraz, Iran

***Corresponding author:** abuzar.shakeri6845@gmail.com

Original Research

Received:
06 July 2025

Revised:
28 September 2025

Accepted:
04 November 2025

Publish online:
31 December 2025

Abstract

In this research, we explore the similar features of quantum dots and quantum wells that function as the optical gain materials in lasers. By utilizing the method of analogy, it allows for a clearer and more analytical interpretation of quantum well lasers, which are more complex than quantum dot lasers. To establish an intuitive picture of conventional lasers with spin-unpolarized carriers and, subsequently, include the influence of spin polarization in spin-lasers, we use a simple bucket model , previously considered only for conventional lasers . Water added to the bucket represents the injection of carriers in the laser, while the water coming out corresponds to the emitted light. The small holes represent carrier losses by spontaneous recombination and the large opening near the top depicts the lasing threshold. In the article, we first discuss the time-dependent rate equations and occupation probabilities related to the rate equations model for classical and spin states of quantum dot lasers and quantum well lasers. The crucial insight in linking the two types of lasers is that the effect of restricted capture time in quantum dot laser function can be accurately mirrored by a suitable choice of the gain compression coefficient in quantum well lasers. Next, we present the two classes of analogies concerning the steady state and dynamical operation separately and explain their restrictions. Finally, we examine the differences between these two analogy models, since the two analogies are not identical, and we extend the correlation to spin lasers

Keywords: Laser; Spintronic; Quantum dots; Quantum wells; Optical gain

1. Introduction

Semiconductor lasers with quantum well (QW) structure can display rich nonlinear dynamic behaviors under external optical injection, optical feedback or optoelectronic feedback, including chaos, switching and bistability [1]–[10]. These nonlinear dynamic behaviors have received considerable research interests because of their potential applications in secure communications, radio-over-fiber communication networks, random bit levels for the carriers,which results to some excellent properties of the QDLs, including low threshold current density, low relative intensity noise, and good temperature stability [22]–[25].

number generation, reservoir computing, photonic neuron, photon microwave signal generation and beam forming [11]–[15]. Low-cost, uncooled, directly modulated and isolator-free laser light sources play a vital role in the next generation of telecommunication links and photonic integrated circuits. As a consequence, Semiconductor lasers based on low-dimensional heterostructures such as QDLs are the promising candidate [16]–[21]. The three-dimensional confinement of quantum dot gives rise to discrete energy

Relevant studies have shown that by choosing the devices length or operating parameters, the QDL can emit from the ground-state solely (GS-QDL), from the excited-state solely (ES-QDL), or from both GS and ES

simultaneously (two-s-tate QDL) [26]–[29]. Up to now, there have some reports on the nonlinear dynamics of the QDL operating at different lasing states under external perturbations. For the GS-QDL subjected to optical injection or optical feedback, the exciting pulses, periodic square wave oscillations and regular pulse packets are generated [30]–[33]. For the ES-QDL under external perturbations, the chaos, quasi-chaotic pulse packets, periodic states, and quasi-regular pulses are exhibited [34],[35].

In addition, for the two-state QDLs that we are focused, Virte et al.have studied the switching behavior of the two-state QDLs under external optical feedback, and found the repetitive but incomplete switching phenomenon between the two emission states when the external cavity length changes on the submicron scale. They have well reproduced the experimental results by using asynchronous electron-hole dynamic model, and pointed out that the potential physical mechanism for switching behavior is the evolution of gain difference between the two emission modes when the feedback phase is changed [36]. In addition, this team have also studied the influence of feedback intensity on the responses of the two-state QDL and found that the laser undergoes a series of dynamics including steady state, external cavity mode, self-pulsation and chaos as the feedback strength gradually increases [37]. Moreover, Tykalewicz et al. experimentally realized a fast all-optical switching based on a two-state QDL subject to optical injection, where the laser is operating at the ES and the frequency of the injected light is close to the emission frequency of GS. By optimizing the injection parameters, the relative suppression ratio of the two modes can be reached to 40 dB and the switching time can be reduced to several picoseconds [38]. It is worth mentioning that this fast switching behavior is similar to the spike neurons in artificial neural networks, and it has a wide application prospect in neural communication [39]. By using the same experimental structure, they also observed the hysteresis and bistability of the two lasing states [40]. Additionally, S. Meinecke and L. Olejniczak et al. have found the bistability and switching behaviors in the two-state QDL under optical injection when the laser is operated at GS or both two states, where the frequency of the injected optical is closed to the GS lasing frequency [28],[41]. Fig. 1 depicts the dynamics of carriers and the arrangement of energy levels of the 2-state QDL. As can be seen from the figure, carriers are injected straight into reservoir state (RS), and later, a portion of the carriers are trapped into ES via Auger and phonon-assisted scattering mechanisms, the capture time is shown by τ_{ES}^{RS}. Moreover, certain carriers in the ES can move to GS via the relaxation phenomenon, where the relaxation time is denoted as τ_{GS}^{ES}. Simultaneously, carriers situated in ES (GS) will transit to RS (ES) because of thermal excitation, with the escape duration denoted as τ_{RS}^{ES} (τ_{ES}^{GS}) [16]. The model overlooks the transition from RS to GS and utilizes the cascade relaxation channel for the carriers. Stimulated emission can produced simultaneously in both GS and ES. In addition to these features of classical (spin unpolarized) QDLs, the prolonged spin relaxation times [17], common in quantum dots, are advantages for spin lasers.

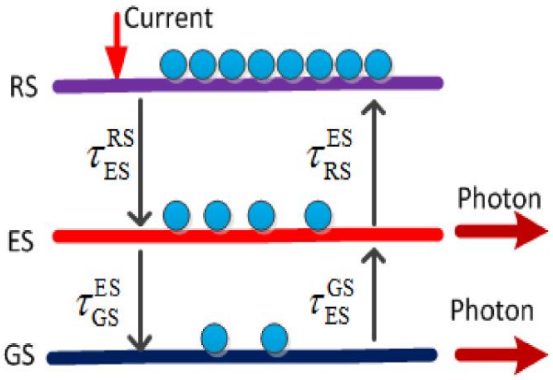

Figure 1. Illustration of carrier behavior and energy level configuration of the 2-state QDL

Fig. 2 illustrates a schematic interpretation of the QWL and QDL. This figure presents the conduction band along with characteristic phenomena encompassed in the rate equation model [17]–[19]. Assuming charge neutrality, the foundational idea is simplified as the explicit inclusion of holes is not needed for classical lasers [17].

The spin polarized injection carriers induce left circularly polarized emission [20]-[27]. Themechanism of carrier recombination (for both quantum wells and quantum dots) may happen either spontaneously or via stimulation, and sufficient injection triggers lasing when the optical gain exceeds the losses inside the cavity of a resonant. A more intricate explanation of QDLs encompasses several extra phenomena and a two-dimensional quantum well resembling a wetting layer, which serves as a carrier reservoir [28]-[30]. Carriers from the wetting layer are either captured by the quantum dot or may escape from the quantum dot back to the wetting layer. To accurately characterize the low density of quantum dot states and the saturation of the wetting layer states at elevated injection levels, it is crucial to incorporate the Pauli exclusion principle [31], which impeded carrier transfer to states close to saturation. The Pauli exclusion principle leads to excess nonlinear effects in the quantum dot rate equations and produces a dark current, such that it is ignored in our explanation of QWLs.

$$P_J = \frac{J_+ + J_-}{J} \tag{1}$$

Here $J_{\pm}$ denotes the two spin projections injection, such that the total injection is $J = J_+ + J_-$. The difference in levels between cold and hot water (refer to Fig. 3b) causes to 3 operational modes and 2 separate lasing thresholds $J_{T_{1,2}}$ [16].

When pumping is low (with cold and hot water levels below the big gap), both up and downward spin carriers remain in the off state, resulting in very low emissions. At more pumping, the hot water arrives at the large opening and spills out, as shown in Fig. 3b, while the flux of cold water released remains negligible.

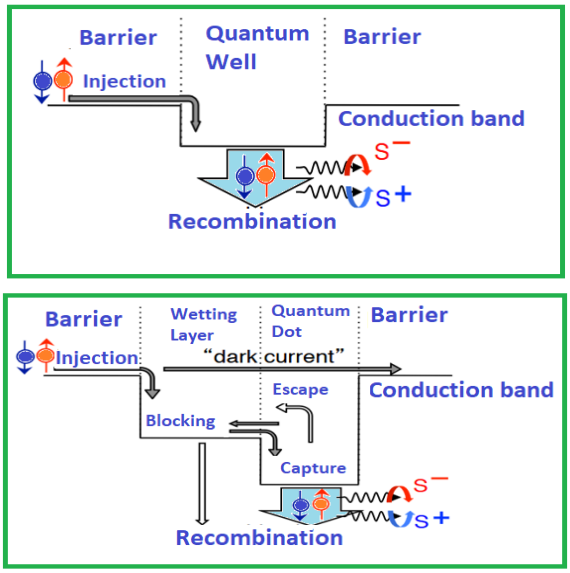

Figure 2. Conduction band diagram and characteristic processes in semiconductor lasers. (a) QWL. A preferential spin alignment of the injected carriers, leads, through electron-hole recombination,to circularly polarized emitted light ($S^{\pm}$ are the emitted photons with positive and negative helicity, respectively). (b) QDL contains an additional level arising from the wetting layer (WL) as well as several more processes,not present in QWLs

This scenario indicates a state where the majority spin is exhibiting lasing, while the minority spin remains inactive; thus,, stimulated emission results from majority spin carriers recombination. Two major effects of this regime have been experimentally confirmed: (1) A spin laser will start lasing with a lower total injection compared to a classical laser (only a segment of the bucket must be filled). This signifies the decrease in thresholds for spin lasers [33]-[35]:

$$r = \eta - J_{T_1}/J_T \qquad (2)$$

Here J_{T_1} denotes the threshold for the majority spin $J_{T_1} < J_T$.Notice that $P_J \leq 1$ can cause high circularly polarized light [22]. The comparative scope of this "spin-filtering region" can be characterized as [18]:

$$d = J_T^{-1}\,(J_{T_2} - J_{T_1}) \qquad (3)$$

Here J_{T_2} represents the threshold for minority spin $\left(\left(J_{T_1} < J_T < J_{T_2}\right)\right)$ leads to the emission of minority helicity photons from the minority of spin carriers, and the light's spin polarized nears $(-P_J)$ as the injection rises [32], akin to the case where cold and hot water exit simultaneously.

QDLs exhibit improved properties compared to QWLs like higher temperature stability, lower threshold current density, and significantly reduced laser line width. This study aims to further optimize QDL morphology and optical material properties in order to narrow the gain spectrum of the ground state transition, improving the laser performance.

QDLs, renowned for their low threshold currents, temperature stability, low-noise optical amplification, and enhanced coherence, are highlighted as essential components for scalable quantum systems.

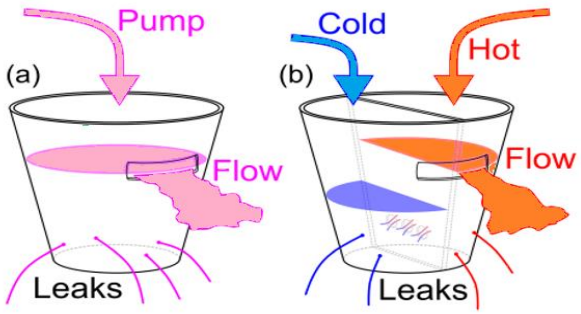

Figure 3. Bucket design for (a) a classical and (b) a solid-state laser. Water being poured into the bucket illustrates the carriers, while the water that overflows depicts the emitted light. Minor leaks signify spontaneous emission, whereas water pouring out from the wide opening represents the threshold of lasing threshold. In part (b), the two compartments represent 2-spin populations (similar to cold and hot water) and each part filled independently. The color scheme illustrates that unpolarized pumping (pink) represents a balanced combination of two polarized components (orange and blue)

QDLs, renowned for their low threshold currents, temperature stability, low-noise optical amplification, and enhanced coherence, are highlighted as essential components for scalable quantum systems. These features contribute to improved chip architectures, reduced module sizes, and increased channel density.

The innovation of this paper is the comparison of quantum well and quantum dot spin-polarized lasers from a dynamic and static perspective by examining the effects of various existing physical phenomena. The physical concepts examined in this article are the determination of carriers escape ratio, carriers capture ratio, carriers' injection, occupation probabilities, photon density, threshold current, response function, peak position frequency, bandwidth frequency, dynamical gain, polarization modulation response function, and amplitude modulation response function.

In accordance with the intuitive diagrams we state here, we will present the rate equations for QDLs and QWLs in the next section. The rate equations solutions in both the steady state and dynamical operation cases offer two methods for the analogy(It should be noted that we have solved the nonlinear differential equations of quantum dot and quantum well lasers in both normal and spin modes through the Runge-Kutta method using Maple software).

In section 3, we focus on the steady state analogy. While section 4 is focused on the dynamical properties of classical lasers. We examine the distinctions between the two mapping techniques in section 5 as the two correlations do not match one another. In sections 6 and 7, we describe spin lasers. Finally, we conclude our study and suggest possible methods for future investigation.

2. Rate equations for classical lasers, QWLs and QDLs via spin injection

2.1. Rate equations for classical laser

In this research, we explore rate equations that have been successfully applied to illustrate both classical and spin

lasers [36]-[40]. An important benefit of this approach is its straightforwardness. rate equations can create a direct link between material properties and device specifications [29], often offering analytical solutions and acting as a helpful tool to elucidate various trends in laser performance [19]. For classical QWLs, we used rate equations for photon (S) and carrier (n) density, respectively [1]:

$$\frac{dn}{dt} = J - g(n,S)S - R_{sp} \tag{4}$$

$$\frac{ds}{dt} = \Gamma g(n,S)S + \Gamma\beta R_{sp} - {S}/{\tau_{ph}} \tag{5}$$

Here the neutrality of charge was applied to cancel the holes rate equations. To define stimulated emission, the optical gain component is denoted by [1]:

$$g(S,n) = g_0(n - n_{tran})/(1 + \epsilon S) \tag{6}$$

In this context, g_0 denotes the gain coefficient [12], n_{tran} indicates the transparency density where the optical gain equals zero, and ϵ symbolizes the gain compression coefficient [41]-[43]. The spontaneous recombination R_{sp} may show various density dependences; in this discussion, we focus on the quadratic expression Bn^2 [44], with B being a temperature-dependent coefficient. Γ represents the optical confinement coefficient, due to various resonant cavity volumes and the laser's active region [1].

β is the spontaneous emission coefficient (β→0) is a precise approximation since experimental values of β (β~$1/100000 - 1/10000$) do not significantly change laser properties, though they do slightly complicate the interpretation of the threshold [45]. The lifetime of photon,τ_{ph}, signifies optical dissipation such as absorption in the boundary materials, dissipation in the mirrors and scattering of photons [46]. According to scrutiny rate Eq. (4), (5) and the optical gain Eq. (6), we find that rate equations are exponentially increased on the variations of t from zero to 50 for n (number of photon carriers), as well as for S (photon density) is negligible in relation to t, This means that n is increased more than S ratio to t.

2.2. Rate equations of spin lasers

For describe QDLs, the use of occupied densities instead of densities and capacity photon is more appropriate [29],[30] .The description of rate equations of QDLs according to Fig. 2b is more complicated than rete equations used QWLs Eq. (4) and (5). Rate equations for QDLs, it is written as:

$$\frac{dn_{\pm}}{dt} = -R_{sp}^{\pm} - g_{\pm}(n_{\pm}.S^{\pm})S^{\pm} + J_{\pm} - (n_{\pm} - n_{\mp})/\tau_s^n \tag{7}$$

$$\frac{ds^{\pm}}{dt} = -{S^{\pm}}/{\tau_{ph}} + g_{\pm}\Gamma(n_{\mp}.S^{\pm})S^{\pm} - \beta\Gamma R_{sp}^{\mp} \tag{8}$$

Here the $\mp$ superscript (subscript) denotes the corresponding photon helicity (electron spin). In Eqs. (7) and (8), a new term exists, which vanishes at $P_J \cong 0$ in classical lasers, linked to spin relaxation: $F = (n_{\pm} - n_{\mp})/\tau_{Sn}$, here τ_{Sn} denotes the electron spin relaxation time. Also, spontaneous recombination is represented by $R_{sp}^{\pm}$=$2Bp_{\pm}n_{\pm}$. The immediate relaxation of hole spin $\tau_{sp} \to 0$ enables us to represent the hole density based on electron densities: $p_+ = p_- = p/2 = (n_+ + n_-)/2$, leading to $R_{sp}^{\pm} = B(n_+ + n_-)n_{\pm}$, assuming charge neutrality holds.In review of the RE for the spin lasers according to Eq. (7) and (8), we find that electrons spin number in the positive and negative states increased exponentially. Also, changes electrons spin number from electron's helicity numbers in the positive and negative states are higher relation to t. Electron's helicity in both states, there is a negligibly increased relation to t.In this section, we compare the obtained result from solving rate equations for classical and spin lasers according to Fig. 4 and 5 and Table. 1. As can be seen from Fig. 4 ,the time variations of n in the classical lasers are higher than S, while both of them initially by increasing time nonlinearly are increased and then trend to a constant value. It can be seen from Fig. 4 and the numerical values in Table. 1 that the values of n correspond to the values of s. The red curve represents the carrier density (n). It starts at a high initial value and rapidly decreases, eventually stabilizing at a constant level.The green curve represents the photon density (S). It begins near zero, increases sharply, and saturates after some time. The steady-state is reached after approximately $t \approx 20 - 30\,s$, where both densities become nearly constant.This behavior reflects the carrier-to-photon conversion process: carriers are consumed to produce photons during stimulated emission. As the laser reaches equilibrium, the gain equals the losses, and both densities stabilize. Also , Fig. 5, shows that the time variations of photon and carrier densities for the upward spin case are similar to those for the downward spin case; however, in both instances, the carrier densities surpass the photon densities and as expected, these quantities initially increase over time and then stabilize after approximately 5 seconds. (see Table. 1). In spin lasers, injected spin-polarized carriers lead to spin-dependent optical gain, causing circularly polarized light emission. The system stabilizes with distinct spin populations for carriers and photons, unlike the symmetric behavior in classical lasers. In summary, Fig. 4 depicts the standard relaxation oscillation toward steady-state lasing, while Fig. 5 reveals spin-resolved dynamics**,** highlighting the emergence of spin-dependent optical gain and polarization in spin lasers.

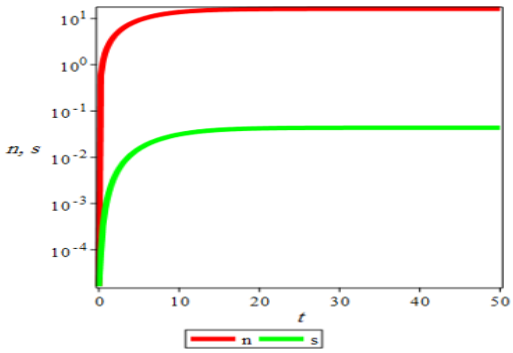

Figure 4. Time variations of carrier (n) and photon (S) densities in the classical lasers

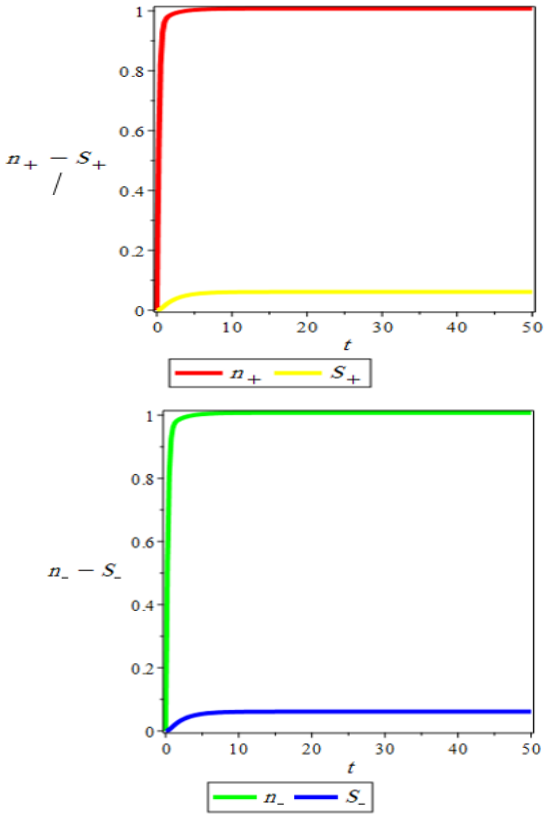

Figure 5. Time variations of carrier ($\boldsymbol{n_-}, \boldsymbol{n_+}$) and photon ($\boldsymbol{S_-}, \boldsymbol{S_+}$) densities for spin lasers

2.3. The occupancy probabilities time dependent in the rate equation model for classical lasers

To define QDLs, it is more suitable to apply occupancies rather than photon and carrier densities, [29],[30]. The rate equations that illustrate the QDLs Fig. 2b are more complex than Eq. (4) and (5), which are utilized for QWLs. In this section, we outline their limiting scenario for classical lasers as follows,

$$\frac{df_w}{dt} = I + \frac{2}{\mathcal{K}}E - C - R_w \tag{9}$$

$$\frac{df_q}{dt} = -E - R_q - G + \frac{\mathcal{K}}{2}C \tag{10}$$

$$\frac{df_S}{dt} = \Gamma_{QD}G + \Gamma_{QD}\beta R_q - {f_S}/{\tau_{Ph}} \tag{11}$$

Here, $\mathcal{K} = \frac{N_w}{N_q}$, where N_w is the number of states in the wetting layer and N_q is the number of quantum dots (each dot contains a twofold spin degenerate level) . The indices q and w denote the quantum dot and wetting layer zones, whereas the index S is associated with photons. The occupancies of holes (occupancies for electrons were excluded based on the neutrality of charge and the assumption that the escape and capture times for holes and electrons are identical) $0 < f_{w,q} < 1$ are linked to the electron's density $\bar{n}_{w,q}$, as $f_w = \frac{\bar{n}_w}{N_w}$ and $f_q = \frac{\bar{n}_q}{2N_q}$. Here, we use an overbar to distinguish numbers from the corresponding densities used in Eqs. (4-6). The photon occupancy: $f_S = \frac{\bar{S}}{2N_q}$, where is $\bar{s}$ the number of cavity photons, does not have an upper bound. In Fig. 6, we plotted the temporal evolution of the occupation probabilities in the rate equations approach for QWLs and QDLs in the classical states. As can be seen, by increasing t initially, all of f_w, f_q, f_s are increased and then reach to a constant value. Also, our computations show that: $f_q > f_w > f_s$. The results from Fig. 6 show how carriers are initially captured from the wetting layer into the quantum dots and how equilibrium is established between the two states. The higher steady-state occupation in QDs reflects their stronger carrier confinement and lower energy levels, which attract electrons from the QWL region.

Table 1. Numerical solutions of rate equations versus time for classical and spin lasers

t(s)	0	10	20	30	40	50
$n(cm^{-3})$	0	13.761	15.981	16.176	16.190	16.191
$n_+(cm^{-3})$	0	1.007	1.007	1.007	1.007	1.007
$n_-(cm^{-3})$	0	1.007	1.007	1.007	1.007	1.007
$S(cm^{-3})$	0	0.031	0.042	0.043	0.043	0.043
$S_+(cm^{-3})$	0	0.060	0.061	0.061	0.061	0.061
$S_-(cm^{-3})$	0	0.060	0.061	0.061	0.061	0.061

The capture and injection of carrier from the wetting layer to quantum dots are represented as $C = f_w {(1 - f_q)}/{\tau_c}$ and , $I = j(1 - f_w)$ where τ_c indicates signifies the capture time, while j is the injected electrons (carriers) numbers into the laser per time per wetting layer state. An inverse of carrier capture is their escape process: $E = {(1 - f_w)f_q}/{\tau_e}$, with τ_e representing the time of escape. These mechanisms incorporate a distinctive Pauli blocking coefficient: (1-f), which is missing in the examination of QWLs, as demonstrated in Eqs. (4) and (5).

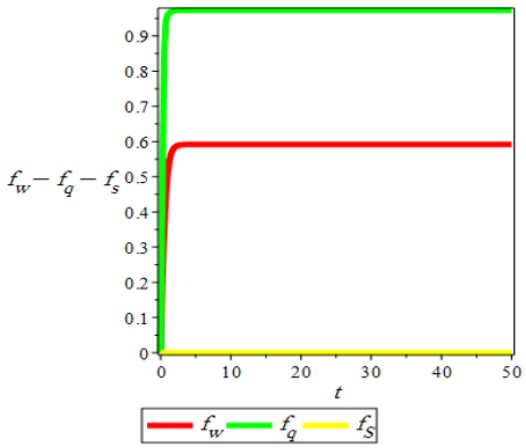

Figure 6. the occupation probabilities time dependency in the rate equations approach for QWLs and QDLs in the classical states

An inverse of carrier capture is their escape process: $E = {(1 - f_w)f_q}/{\tau_e}$, with τ_e representing the time of escape. These mechanisms incorporate a distinctive Pauli blocking coefficient: (1-f), which is missing in the examination of QWLs, as demonstrated in Eqs. (4) and (5).

It is important to acknowledge the nonlinear characteristics of capture and escape terms C, E in quantum dots. The lack of these nonlinearities in QWL Rate equations offers an additional simplification in understanding QDLs through the analogy method, allowing for a more straightforward explanation. Additional processes represented in Fig. 2b consist of the recombination of spontaneous radiative $R_\eta = f_\eta^2 b_\eta$, with $\eta = q, w$. The neutrality of charge signifies that f_η^2 essentially pertains to the product of hole and electron populations [18]. The light and carrier coupling in Eqs. (8) and (9) represent stimulated emission, which can be expressed by:

$$G = -(1.0 - 2f_q)gf_S \qquad (12)$$

where g remains unaffected by photon occupancies and does not incorporate the gain compression coefficient, ϵ, employed in the QWLs. Applying occupancies instead of densities for quantum dot rate equations eliminates several volume factors, and there is no necessary to incorporate the optical confinement coefficient ($\Gamma_{QD} = 1.0$)that is needed in the Eqs. (5). Lastly, τ_{ph}resembles the variable that has been previously used in Eq. (5).
Here, according to review and assessment Table. 2, we reviewed first carrier capture and the escape for QWLs, then carrier injection and, at the end, responsible for stimulated emission.

We find out that in the states f_w constant and f_q changes between 0 to 1, carrier escape increases and carrier capture decreases, therefore E and C act on the inverse. In Fig. 7, we plotted the 3D variations of carriers escape ratio to electron occupation in the wetting layer and quantum dot regions .From this figure we find that by reducing f_w and increasing f_q ,E is increased. The results from Fig. 7 visualize the dynamic equilibrium between carrier capture and escape processes**.** Efficient laser operation requires an optimal balance — too few carriers lead to low photon generation, while too many cause escape losses and saturation. Also,in Fig. 8, we plotted the 3D variations of carrier captuer ratio to electron occupation in the wetting layer. But from this figure we see that by increaing f_w and reducing f_q the C parameter is grown.

The figure demonstrates how carrier capture efficiency depends on the balance between injection and escape dynamics. Optimizing these parameters ensures maximum carrier confinement in QDs, which enhances laser gain and modulation performance**.**

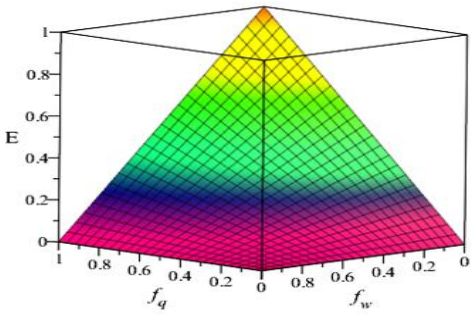

Figure 7. Three dimensional variations of carriers escape ratio to electron occupation in the wetting layer and quantum dot regions

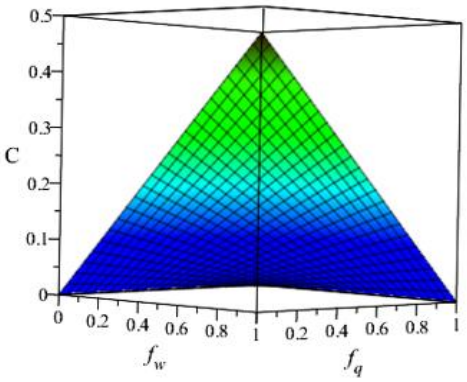

Figure 8. Three dimensional variations of carriers captuer ratio to electron occupation in the wetting layer

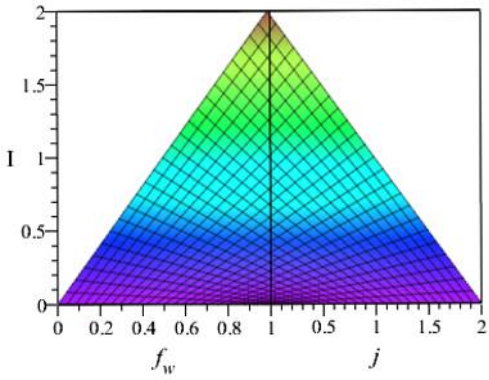

Figure 9. Three dimensional variations of carriers' injection in terms of f_w and j

Then according to Table. 2 and Fig. 9, we plotted the 3D variations of carriers' injection in terms of f_w and j.

A can be seen with decreasing f_w and increasing j then carrier injection in creases. In next step, we determined the neumerical vaues of G values in different conditions in Table. 2.

Table 2. Review injection, capture, escape, and the stimulated emission carriers.

f_q	f_w	C (ps^{-1})	E (ns^{-1})	J (ps^{-1})	f_w	I	f_S	f_q	G (cm^3s^{-1})
0		0	0	0		0	0		0
$\frac{1}{2}$		0	$\frac{1}{2}$	1	0	1	$\frac{1}{2}$		-0.008
1	0	0	1	2		2	1	0	-0.0016
0		0.250	0	0		0	0		0
$\frac{1}{2}$		0.120	$\frac{1}{4}$	1		$\frac{1}{2}$	$\frac{1}{2}$		0
1	$\frac{1}{2}$	0	$\frac{1}{2}$	2	$\frac{1}{2}$	1	1	$\frac{1}{2}$	0
0	0.5		0	0		0	0		0
$\frac{1}{2}$		0.250	0	1		0	$\frac{1}{2}$		0.008
1	1	0	0	2	1	0	1	1	0.0016

2.4. Occupation probabilities time dependency-using rate equation for spin laser

A key difference between the rate equations of QW spin lasers and QD spin lasers is that only QD spin laser rate equations incorporate explicit components for the occupancies of hole. In QW spin lasers, The density of the hole can readily be substituted by the density of electron as mentioned earlier $\tau_{sp} \to 0$. Nevertheless, in the case of quantum dots, unlike quantum wells, the extremely fast spin relaxation time for holes $(\tau_{spw}, \tau_{spq} \to 0)$ does not remove the clear hole density dependence found in quantum dot rate equations. This makes the analytical analysis of quantum dot spin lasers more complex, even in the steady state. A broader interpretation of the quantum dot Eqs. (9-11) for spin lasers represents:

$$\frac{df_{w\alpha\pm}}{dt} = \frac{2}{\kappa_\alpha} E_{\alpha\pm} + I_{\alpha\pm} \mp f_{w\alpha} - R_{w\pm} - C_{\alpha\pm} \qquad (13)$$

$$\frac{df_{q\alpha\pm}}{dt} = -E_{\alpha\pm} - G_{\pm} - R_{q\pm} \mp f_{q\alpha} + \frac{\kappa_\alpha}{2} C_{\alpha\pm} \qquad (14)$$

$$\frac{df_{S\mp}}{dt} = G_{\pm} - {f_{S\mp}}/{\tau_{Ph}} + \beta R_{q\pm} \qquad (15)$$

Here $\alpha = p, n$ represents holes and electrons ,respectively. R, E, G, C, and I refer to spontaneous emission, escape, stimulated emission, capture, and injection, respectively, as observed in unpolarized rate equations whereas F indicates spin relaxation. Fig. 10 shows the energy level diagram of a QD spin laser.

As the occupancies satisfy the condition: $0 \le f_{w,q} \le 1.0$,, the spin polarized occupancies are expressed by: $f_{w\alpha_\pm} = \frac{\bar{n}_{w\alpha_\pm}}{(N_{w\alpha}/2)}$, $f_{q\alpha_\pm} = \frac{\bar{n}_{q\alpha_\pm}}{N_q}$ and $f_{s_\pm} = {S_\pm}/{N_q}$, differing from Eqs. (9-11) by a factor of 2.0. The parameters for capture, escape and carrier injection are expressed as $C_{\alpha_\pm} = f_{w\alpha_\pm} \frac{1-f_{\alpha_\pm q}}{\tau_c}$, $E_{\alpha_\pm} = f_{q\alpha_\pm} \frac{1-f_{w\alpha_\pm}}{\tau_e}$, and

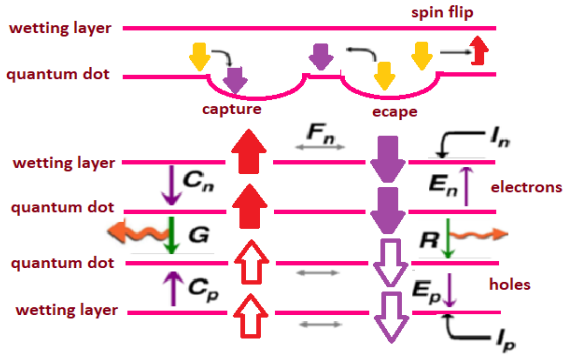

Figure 10. Processes in our model of a spin-laser, described by Eqs. (13-15). Upper panel: thick arrows denote electron spin direction in processes labeled by their corresponding times. Lower panel: thick vertical arrows show the carrier spin (filled for electrons, empty for holes). Curved arrows show carrier injection I. Thin arrows depict capture C, escape E, spin relaxation F, stimulated (G) and spontaneous (R) recombination (thickness indicates relative rates). The subscripts n and p represent the electron and hole contributions, respectively. Wavy arrows depict photon emission

$I_{\alpha_\pm} = j(1 - f_{w\alpha_\pm}), C_{\alpha_\pm}$,with the injection of $j_{\alpha\pm} = (1 \pm P_{j\alpha})j_\alpha$ represented in relation to the associated spin polarized: $P_{j\alpha} = \frac{j_{\alpha+} - j_{\alpha-}}{j_{\alpha+} + j_{\alpha-}}$. The formulas for spontaneous and stimulated emission are $R_{\eta\pm} = b_\eta f_{\eta n\pm} f_{\eta p\pm}$ and $G_\pm = g(f_{qn\pm} + f_{qp\pm} - 1) f_{S\pm}$,respectively, b_η representing the recombination rate and with η=w,q. The expression for spin relaxation is $f_{\eta\alpha} = \frac{f_{\eta\alpha+} - f_{\eta\alpha-}}{\tau_{s\alpha\eta}}$, with $\tau_{s\alpha\eta}$denoting the spin relaxation time. In this research, we consider that $\tau_{sn\eta} = \tau_s$, $\tau_{sp\eta} = 0$, $\beta = 0, J_\alpha = J, \tau_{C\alpha} = \tau_C$, $\tau_{e\alpha} = \tau_e$, and $P_{j\alpha} = P_j$.

Now, we examine the time variations of the electrons, photons and holes occupation probabilities using rate equations for QDLs and QWLs, encompassing both classical lasers and spin lasers. Consequently, we determined the time-dependent development of the electron's occupation probabilities in the wetting layer and quantum dot zones at the end of the time variation of the occupation probabilities of photons. At this point, only the probabilities of occupation for electrons and photons are taken into account. We notice that the time-

dependent variations in the occupation probabilities of electrons in the quantum dot zone are more pronounced compared to the wetting layer, and this change is approximately 1, with f_S being zero. Afterward, the time-dependent variations in the electrons, photons, and holes occupation probabilities within the wetting layer and quantum dot zones are examined according to Fig. 11, incorporating the processes of capture, injection, escape, spontaneous emission, and excitation of carriers in the spin state. Overall, the figure illustrates that the system quickly stabilizes into a steady-state distribution of spin-resolved carrier and photon populations, a typical behavior in rate-equation models for spin lasers.

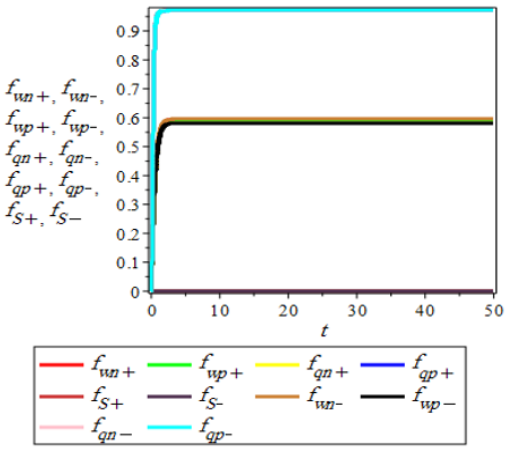

Figure 11. time variations of the occupation probabilities using rate equations approach for spin lasers

Here, we deduce that the time variations of the occupation probabilities for upward spin electrons in the wetting layer are 0.002 fewer than the downward spin electrons. Nonetheless, 0.002 surpasses the time progression of the occupation probabilities for holes with upward spin in the wetting layer. The time variations of the occupation probabilities for downward spin holes in the wetting layer are roughly 0.009 from the upward spin state in the holes and approximately 0.015 from the distribution of electrons in the temporal progression of the occupation probabilities for electrons with both upward spin and downward spin states in the wetting layer. Next, we examine the temporal development of the hole and electron's occupation probabilities with both up and downward spin in the quantum dot zone. Here we find that the temporal evolution of the occupation probabilities of electrons and holes in the up and downward spin increases more than the temporal evolution of the occupation probabilities electrons and holes in the up and downward spin in the wetting layer, and it's like classical lasers close to one. The temporal evolution of the occupation probabilities electrons with upward spin and downward spin in the wetting layer both are the same size, and from the temporal evolution of the occupation probabilities holes with upward spin at quantity 0.001 and with downward spin is greater than quantity 0.002. Finally, with reviewing the temporal evolution of the occupation probabilities of photons, we can see that, like classical lasers, are zero.

3. Steady state analogy

In alignment with the rate equations specified in Sec. 2, we examine the potential for establishing a correlation between QDLs and QWLs. Our aim is to obtain an approximately solution for the complex QDL rate equations utilizing the solutions obtained from the rate equations of QWLs. To create the analogy, two conditions must be met for the correlated QWL rate equations. To start, the rate equations ought to precisely compute stationary-state charasrtristics like light intensity and threshold. Simultaneously, the dynamical characteristics of lasers need to be depicted by the rate equations using different numerical or analytical methods such as small or large signal analyses. In this part, as a first step, we focus on the steady state performance for which the quantum well correlated parameters are obtained from the quantum dot properties by analytical solution of Eqs. (4), (5) and (11-13), while τ_{ph} and β remain unchanged for QDLs and QWLs. Ideally, the subsequent equations should be valid:

$$\mathrm{J} = \left(\frac{N_q}{V}\right)\mathcal{K}\mathrm{j} \tag{16}$$

$$\mathrm{n} = \left(\frac{N_q}{V}\right)\left[2\mathrm{f_q} + \mathcal{K}\mathrm{f_\omega}\right] \tag{17}$$

$$\mathrm{S(J)} = 2\Gamma\left(\frac{N_q}{V}\right)\mathrm{f_s(j)} \tag{18}$$

As stated in Eq. (16) and Fig. 12, we can conclude that when the electron states numbers in a quantum dot zone remain fixed and j varies from 0 to 10, then $J(j)$ increases, such that the increase of $J(j)$ is greater than all states when the number of electron occupation states within the quantum dot region is equal to $N_q = 100$, and if $N_q = 10$ then, $J(j)$ has the minimum increase. Fig. 12 presents a three-dimensional surface plot illustrating how the parameter J varies as a function of the injection current density j and the quantum-dot carrier number Nq. Physically, the plot demonstrates that J increases with both j and Nq, reaching its maximum value when both parameters are high. The smooth gradient from lower (purple and blue) to higher (yellow and red) color regions indicates a continuous and monotonic dependence of J on these variables. This behavior suggests that higher carrier injection and quantum-dot occupation lead to enhanced optical or electronic gain, a characteristic feature in the operation of quantum-dot spin lasers or similar semiconductor devices.

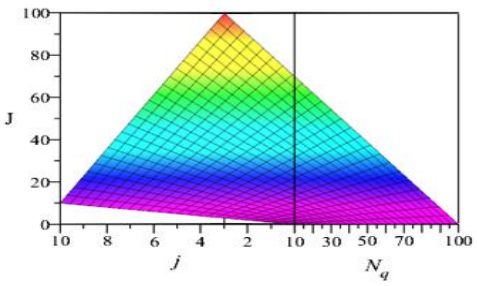

Figure 12. Three dimensional variations of J in terms of j and N_q

Moreover, we plotted the 3D variations of n in terms of f_w (electron occupation in wetting layer) and f_q (electron occupation in quantum dot zone) in Fig. 13. It has been noted that increasing f_w and f_q improves the n value, although a rise in f_q has minimal effect on the n value. Fig. 13 presents a three-dimensional plot illustrating the variation of the electron occupation parameter nnn as a function of two variables: f_w (the electron occupation in the wetting layer) and f_q (the electron occupation in the quantum dot region). The surface shows a linear relationship, where n decreases gradually from its maximum value when f_w is high and f_q is low, to its minimum value as f_q increases and f_w wfw decreases. The color gradient—from red at low n values to yellow at high n values—visually represents this transition, emphasizing how electron distribution shifts between the wetting layer and the quantum dot region affects the total occupation number n.

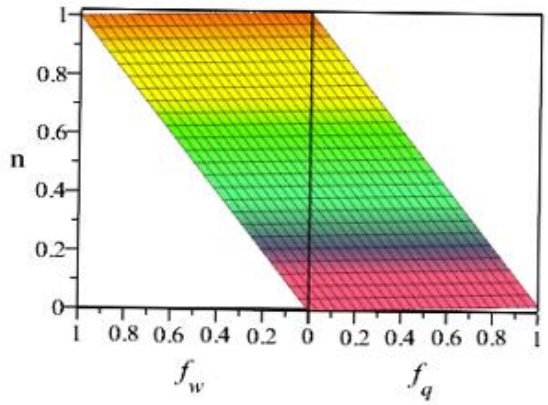

Figure 13. Three dimensional variations of n in terms of (a) f_w(electron occupation in the wetting layer) f_q(electron occupation in the quantum dot region)

According to Eqs. (22) and (23), we consider changes n according to the temporal evolution QWLs and QDLs rate equations in the wetting layer and quantum dots region.

We first consider three constant states for f_q, that by examining these states, we find that in all states, n increases to an equal magnitude. Then we again calculate, n changes in the states where f_w is constant and $f_q$change. According to the calculations done, we find that in all states there is an increase of 0.2. Here we compute the variations of S according to Eq. (18), which is shown in Fig. 14. From this figure we conclude that photon density increases with increasing f_S .

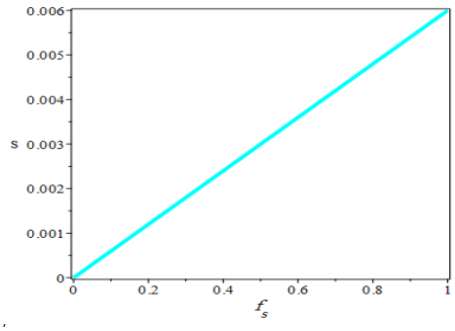

Figure 14. variations of photon density (***S***) in terms of photon occupation (f_S)

In Eqs. (16-18), V stands for the active zone volume, and $J(j)$ denotes injection at the rate equations for QWL (QDL). Although Eq. (16) is considered valid by definition, as indicated by the Eqs. (17) and (18) cannot be satisfied for every j. Thus, we establish four issues from the solutions obtained from QWL and QDL rate equations: a) Transparency carrier density$n_{tran} = \left(\frac{N_q}{V}\right)\left[2f_q(j_{trans}) + \kappa f_w\,(j_{tran})\right]$, where j_{trans} is the injection values at transparency and $f_q(j_{tran}) = \frac{1}{2}$ [see Eqs. (6) and (15)]. b) The threshold carrier density $n_T = n_{tran} + \frac{1}{\Gamma g_0 \tau_{ph}} = \left(\frac{N_q}{V}\right)\left[2f_q(j_T) + \kappa f_w\,(j_{tran})\right]$ establishes g_0 (for QWLs), with $j_T$representing the injection (for QDLs) at the threshold. **3)** The threshold current density $j_T$is defined as: $j_T = Bn_T^2 = \kappa\left(\frac{N_q}{V}\right)J_T$, and $j_T$specifies B (for QWLs), with $j_T$representing the injection threshold current for QDL.

4) The density of photon $S = 2\Gamma\left(\frac{N_q}{V}\right)f_s$ defines ϵ_s, with subscript S indicates it was derived in a stationary-state condition. With a constant injection $(j = \alpha j_T)$, the density of photons obtained from the QDL and QWL rate equations are aligned to converge. Here, α=10 is designated.

The pertinent mapping parameters are listed in Table 1. When $\tau_c \to 0$, the wetting layer acts as "transparent" to carriers since the injected carriers are suddenly confined in quantum dots; therefore, under the RE description for $\epsilon_s = 0$, QDLs and QWLs display the same behavior.

In each case, whether $\tau_c = 0$ or $\epsilon_s = 0$,, the carrier density stays constant above the threshold, while the density of photon increases linearly, according to Refs. [1] and [22].

For a finite τ_c (2ps in Fig. 14), the density of the carrier shows an increase, while the density of the photon decreases. If $n > n_T$, the rise in the density of carriers can mainly be attributed to wetting layer occupancy, which increases for $\tau_c > 0$. In the lack of any gain term in Eq. (13) , we can conclude that the presence of the wetting layer does not influence stimulated emission. However, because the active zone is thought to consist of a wetting layer and quantum dots, we address this "inefficiency" of the wetting layer in terms of light emission by incorporating ϵ_s into the QWL model. The usual range of ϵ observed experimentally in QWLs is approximately $\epsilon \sim 10^{-19} - 10^{-17}$ [10] – [12].

In comparison, in our analogy, we apply a notably higher ϵ_s~10^{-14},, which accurately represents the characteristics of QDLs, as demonstrated by the comparison of the lower and upper parts inside in Fig. 14. The assessment of Fig. 14 shows that in a QDL, the influence of a limited τ_c (i.e., raising N and decreasing S with injection) mirrors the consequences of a confined gain compression coefficient ϵ_s in a QWL. This indicates that, in a steady state, by defining ϵ_s based on τ_c, QDL rate equations can be successfully replaced with QWL rate equations. Additionally, it is crucial to recognize that as τ_c increases in QDLs, negative impacts like phonon bottleneck or spectral hole burning will grow, and these nonlinear effects are included by adding 0 to the QWL rate equations.

4. Dynamical operation analogy

The analogy between QDLs and QWLs is useful under steady states, and the influence of finite τ_c, illustrated in Fig. 14, on the injection of light and the density of carrier characteristics is accurately depicted by including a significant ϵ_s in the QWL. Nonetheless, the key characteristics of lasers often pertain to their dynamical functionality, highlighting the importance of assessing whether the previously mentioned analogy holds true in this situation. To tackle this, we employ the classical method of small signal analysis and implement it for both QDLs and QWLs. We separate the relevant variables, X, into a constant part X_0 and a small oscillating component $\delta X(t)$, expressed as $X = X_0 + \delta X(t)$,, and focus on the harmonic oscillation $\delta X(t)$, $X = X_0 + \delta X(t)$, where ω represents the angular frequency. The response function, which defines dynamical performance including the laser bandwidth, is represented by [26]-[28] :

$$R_\omega = \left| {\delta S(\omega)}/{\delta J(\omega)} \right| \tag{19}$$

It is practical to regard the normalized frequency response function [11].

$$\left|\frac{R(\omega)}{R(0)}\right|_{QW} = \frac{\omega_R^2}{[(\omega_R^2 - \omega^2)^2 + \omega^2\gamma^2]^{1/2}} \tag{20}$$

Where $\omega_R^2 \cong g_0 s_0/[\tau_{ph}(1+\varepsilon s_0)]$ is the relaxation oscillation frequency, and γ is a damping factor [41], [42]. The functional form of Eq. (20) is the same as for the amplitude of a harmonically driven damped harmonic oscillator [41] .It is useful to express the damping factor as:

$$\gamma \approx 2Bn_T + K\left[{\omega_R^2}/{(2\pi)}\right]^2 \tag{21}$$

Where the K –factor is

$$K \approx 4\pi^2 + \left(\tau_{Ph} + {\epsilon}/{g_0}\right) \tag{22}$$

Which is a vital parameter that estimates the operation threshold of lasers. In the earlier equations we take into account $\varepsilon \ll {g_0}/{2Bn_T}$. The laser's bandwidth, ω_{3dB}, is defined as the frequency where $|R(\omega)/R(0)|$ square inside Eq. (20) is reduced by $3dB$.Also, ω_{3dB} and ω_R are depend on the injection of steady state J_0, and they correspond with the peak of bandwidth ω_{3dB}^{max}. Usually, the position of peak $\omega_{peak}^2 = {\omega_R}^2 - {\gamma^2}/{2}$ is approximated as ω_R (if $\omega_R \gg \gamma$), whereas QWLs bandwidth may be linked to ω_{peak} and ω_R .

$$\omega_{3dB}^2 = \omega_{Peak}^2 + (\omega_{Peak}^4 + \omega_R^4)^{1/2} \tag{23}$$

The highest bandwidth occurs when: ${\omega_R}^2 = {\gamma^2}/{2}$, leading to a consistent decrease of the response function as specified in Eq. (20). For QDLs, if we consider: $\omega_r \ll \frac{1}{\acute{\tau_c}}$, then $\omega_r(\acute{\gamma}_{QD})$ for a QDL corresponds to $\omega_R(\gamma)$ for a QWL . $\tau_c \approx \acute{\tau_c}/(1-f_{q_0})$ is defined as effective capture time. In this situation, we obtain:

$$\left|\frac{R(\omega)}{R(0)}\right|_{QD} \approx (1+\omega^2\tau_C'^2)^{-1/2} \times \left|\frac{R(\omega)}{R(0)}\right|_{QW} \tag{24}$$

In this context, using the analogy of dynamical operation, we first describe the normalized response function as a function of frequency in QWLs, differing from the classical approach of small-signal analysis. This is demonstrated in Fig. 14. In Fig. 16, we analyzed different scenarios of the normalized response function as a function of frequency in QWLs while keeping ω constant, observing that the response function does not perform well at zero frequency, yet shows its peak position at different frequencies (See Fig. 16). Fig. 15 illustrates a three-dimensional variation of the normalized frequency response function $({\mathrm{R}_\omega}/{\mathrm{R}_0})_{\mathrm{QW}}$ in the wetting layer as a function of frequency ω and relaxation oscillation frequency ω_R. Physically, the plot demonstrates how the response amplitude changes with varying oscillation and driving frequencies. The oscillatory peaks indicate resonance behavior, where the response function reaches maximum values at specific frequency combinations due to coupling between the wetting layer and the relaxation dynamics of the system. As the relaxation oscillation frequency increases, the amplitude of these oscillations gradually diminishes, signifying damping effects and reduced resonance strength at higher frequencies. This behavior reflects the dynamic interaction between the carrier population in the wetting layer and the modulation frequency.

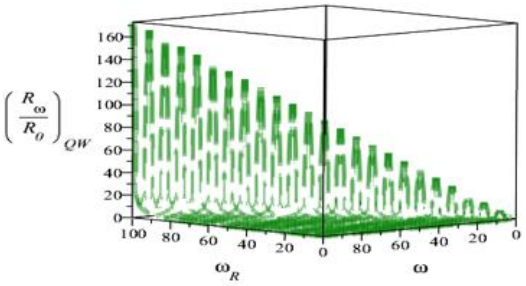

Figure 15. Three dimensional variations of normalized frequency response function in wetting layer in terms of frequency and relaxation oscillation frequency

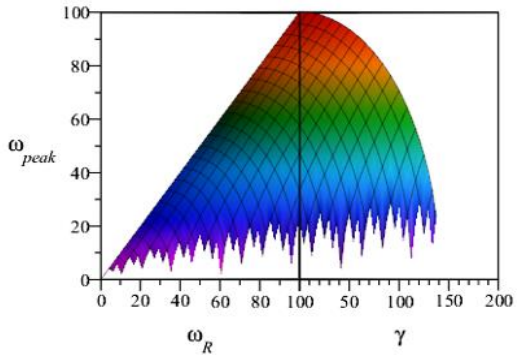

Figure 16. Three dimensional variations of peak position frequency in terms of $\boldsymbol{\omega_R}$ and $\boldsymbol{\gamma}$

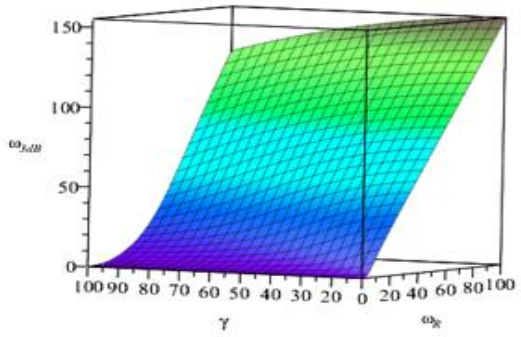

Figure 17. Three dimensional variations of bandwidth frequency in terms of $\boldsymbol{\omega_R}$ and γ

Physically, it demonstrates that ω_{peak} increases with ω_R and reaches a maximum value at an optimal combination of ω_R and γ, after which it decreases as damping becomes dominant. This indicates that while stronger relaxation oscillations enhance the system's resonant response initially, excessive damping suppresses it by broadening and lowering the resonance peak. The curved surface thus captures the balance between oscillation strength and damping in determining the frequency at which the system exhibits its maximum response.

But, the bandwidth frequency with relaxation oscillation frequency increases exponentially upwards (See Fig. 17). Fig. 17 shows a three-dimensional variation of the bandwidth frequency ω_{3dB} as a function of the relaxation oscillation frequency ω_R and the damping factor γ. Physically, the surface illustrates how the modulation bandwidth of the system depends on

In this segment, we investigate the peak position frequency and the bandwidth frequency, considering both of the two modes:

At first, the fixed damping factor, and second the constant relaxation oscillation frequency. In the case of a constant damping factor γ, the peak position frequency and bandwidth frequency both increase. The peak position frequency with relaxation oscillation frequency increases exponentially downwards (See Fig. 16). Fig. 16 presents a three-dimensional plot showing how the peak position frequency ω_{peak} varies as a function of the relaxation oscillation frequency ω_R and the damping factor γ.

these two parameters. As ω_R increases, ω_{3dB} rises sharply at first and then tends to saturate, indicating that higher relaxation oscillation frequencies enhance the system's response speed up to a limit. Similarly, increasing γ broadens the bandwidth initially due to improved damping control, but excessive damping reduces dynamic efficiency. Overall, the figure reflects the trade-off between oscillation strength and damping in determining the maximum achievable modulation bandwidth of the system.

Then, in the state that is constant relaxation oscillation frequency, peak position frequency and bandwidth frequency are both exponentially downtrend, The peak position frequency according to Fig. 16, with increasing damping factor in different states of the constant relaxation oscillation frequency on each graph, reaches a fixed point on the damping curve (see Fig. 16). But, bandwidth frequency with increasing damping factor in different states relaxation oscillation frequency each graph, in the end, reaches a fixed downtrend (see Fig. 17).

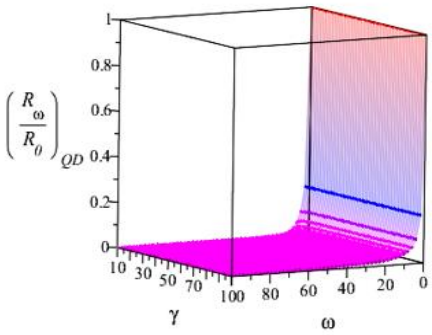

Figure 18. Three dimensional variations of normalized frequency response function in the quantum dot zone in terms of $\boldsymbol{\omega_R}$ and $\boldsymbol{\gamma}$

Fig. 18 shows a three-dimensional plot illustrating the variation of the normalized frequency response function $(^{R_\omega}/_{R_0})_{QD}$ in a quantum dot system as a function of the driving frequency ω and the damping coefficient γ. Physically, the response function represents how the quantum dot's oscillation amplitude or energy absorption changes with these parameters. The surface plot reveals that at low values of γ and ω_R, the response remains nearly constant and minimal, but as either ω or γ increases, the response exhibits a sharp rise, indicating a resonance-like enhancement. This behavior reflects the system's sensitivity to frequency and damping

variations, characteristic of quantum confinement effects influencing the dynamic properties of the quantum dot.According to the normalized frequency response function in quantum well lasers, we can consider the normalized frequency response function for QDLs which, according to Fig. 18, increases the damping factor in the different constant frequencies by the normalized frequency response function exponentially increases, but in the state that $\omega = 20$, such as the yellow graph of the Fig. 18 within a certain range of the axis, has an uptrend and then in the following this uptrend is less, so that almost graphing becomes monotonic, with increasing frequencies, for example $\omega = 40\ ,60$, as green and red graphs of the Fig.

$$(1 + \omega_{3dB}^2 \tau_c'^2)\ [(\omega_r'^2 - \omega_{3dB}^2) + \omega_{3dB}^2 \gamma_{QD}^2] = 2\omega_r'^4 \quad (25)$$

Which, as $\tau_c \to 0$ approaches zero, reverts to the quantum well characteristics defined by Eq. (23). Our rate equations for the QDL are similar to those of separate confinement hetero-structure lasers [44], but in QDLs, the Pauli Exclusion Principle needs to be considered. The Pauli coefficient, represented as: $1 - f_n$, not only decreases the stationary-state photon density but also significantly lowers the modulation response function. [42]-[44] Likewise, as seen in the associated capture in SCH lasers, the effect of τ_c on the quantum dot modulation response function contributes to low frequency roll-off . When $\tau_c$increases to the point where the roll-off dominates, the maximum bandwidth achieved is $\sim \frac{1}{\tau_c}$. Our calculations indicate that for enhancing the QDL dynamical response function, the capture time should be low enough,(i.e $\tau_c < 10ps$) [35]-[39].

As mentioned in Sec. 3, it is required that the mapped QWL rate equations recover the dynamics of QDLs. While our goal is not to fully recover a detailed dynamical response of QDLs, we do require that the maximum band width ω_{3dB}^{max} , as the key figure of merit characterizing dynamical operation, coincides for QDLs and QWLs. This can be achieved through a K-factor that defines the maximum frequency for QWLs and depends on ϵ.

The analogy is then realized by following the same matching procedure and conditions (1)-(3) described in Sec. 3, while the earlier condition (4) is now substituted with the formula for ϵ_d that indicates the matching of the optimal bandwidth from Eq. (22),

$$\epsilon_d \approx g_0 \left({\sqrt{2}}/{\omega_{3dB}^{max}} - \tau_{Ph} \right) \quad (26)$$

Where the subscript d signifies the dynamic response with the related value that does not have to match the value derived in the stationary-state analogy, that is, ϵ_s . The highest bandwidth ω_{3dB}^{max} is computed from the QDL rate equations; Eq. (26) is valid for $\omega_{3dB}^{max} \gg 2Bn_T$ and $\epsilon_d \ll {g_0}/{(2Bn_T)}$.

18, we have an increase in the beginning, but in the middle of these figures, we encounter decreasing and increasing oscillation, and at the end $\omega = 80\ ,100$, like blue and brown graphs of the Fig. 19, Overall, we see an uptrend. But in the state that consider the constant damping factor, In all states, by increasing relaxation oscillation, the frequency of the normalized frequency response function in QDLs exponentially decreases. The quantum dot parameters are $\tau_{Ph} = 2\ ps$, $b_q \tau_{Ph} = 0.01$, $b_w \tau_{Ph} = 2.33$, $g\tau_{Ph} = 2$, $\kappa = 100$ and $\tau_e = 1\ ns$ [47]. Analogously to QWLs, the bandwidth for QDLs can be obtained from the equation:

Fig. 19 presents the variation of the dynamical gain, ϵ_d, as a function of the maximum bandwidth frequency ω_{3dB}^{max} for two different carrier lifetimes, $\tau_c = 0ps$ (red curve) and $\tau_c = 2ps$ (blue curve).

In quantum dot spin lasers, the stationary gain is typically greater than the dynamical gain because, under steady-state (stationary) conditions, carriers have sufficient time to relax and fully populate the lower-energy s-shell states, producing maximum population inversion and hence higher optical gain. In contrast, during dynamic or high-speed modulation, the carrier distribution and spin populations cannot instantaneously reach equilibrium due to finite carrier capture, escape, and spin relaxation times; this results in incomplete inversion and reduced stimulated emission, leading to lower dynamical gain.

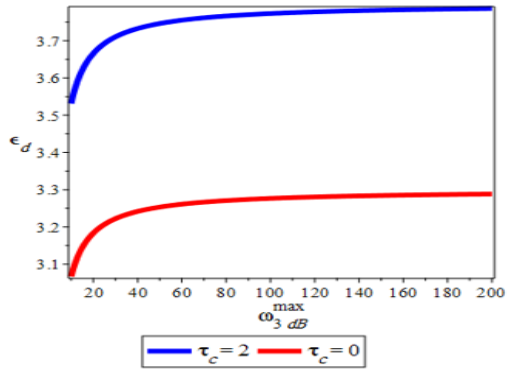

Figure 19. variations of dynamical gain in terms of maximum bandwidth frequency in the $\tau_c = 0$ *and* $2ps$

Similarly, the relation $\varepsilon_s > \varepsilon_d$ reflects that the photon energy associated with the s-shell transition is higher than that of the d-shell (since the s-shell lies deeper in energy), meaning the s-shell emission occurs at a shorter wavelength and generally dominates the steady-state laser operation. Fig. 20, illustrates the variation of the normalized injection current ratio ${J_{T1}}/{J}$ and ${J_{T2}}/{J}$ as a function of the carrier lifetime τ_c (left plot) and the polarization parameter P_J (right plot). Physically, the left graph shows that as $\tau_c$increases, the injection ratio ${J_{T1}}/{J}$exhibits only a slight rise, indicating that the carrier lifetime has a weak influence on the injection process.

In contrast, the right graph demonstrates that ${J_{T2}}/{J}$ increases sharply with increasing P_J, especially near

higher polarization values, signifying a strong dependence of injection efficiency on polarization. This behavior suggests that while carrier relaxation time contributes marginally to the injection dynamics, polarization plays a dominant role in enhancing carrier injection and modulation efficiency within the quantum dot system.

Eq. (26) produces an error of under 3% with $\tau_c = 2ps$ as compares with precise computations [45]. Nevertheless, across a wide spectrum of τ_c, we employed the formulas presented in [45]. To consider the distinctions between the two mapping techniques, we depict in Fig. 19 .The response function of a QDL along with response functions computed for QWLs utilizing both dynamical response and stationary state correlates at a known injection . When τ_c=0, the rate equations for QDLs decrease to the rate equations for QWLs where $\epsilon = 0$. Notice that qualitative similarities regarding finite ϵ and τ_c, both of which are negative and result in bandwidth suppression.

In the analysis of a small signal, the derived QWL response function represents a wider distribution and various slope in the tail compared to QDLs. As indicated in Fig. (19), using the gain compression coefficient acquired from the stationary state analogy, ϵ_s, results in a poor approximation of the response function for a QDL.

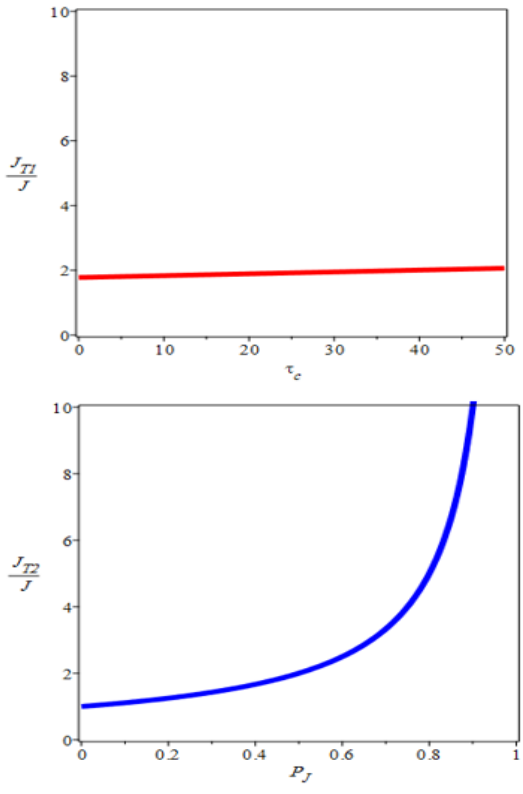

Figure 20. variations of injection $\frac{J_{T1,2}}{J}$ in terms of τ_c and P_J

The correlation improves considerably when a notably smaller gain compression coefficient from the dynamical operation analogy, ϵ_d, is used instead. We observe that the response functions of the quantum dot and QW are nearly identical up to ~10GHz (the highest bandwidth match for high currents).

To evaluate the effectiveness of the dynamical operation analogy, we present the injection dependence of the bandwidth ω_{3dB} and the peak position ω_{Peak} for the quantum dot and QWLs in Figs. 21 and 22. It is important to highlight that the analogy specifically created to match the highest bandwidth between the QDLs and QWLs, shows remarkable consistency with how the bandwidth depends on injection. Both quantum dot and quantum well situations display non-monotonic behavior up to $J \sim 6J_{T_0}$.

While Fig. 18, illustrates a very comparable peak position for QDLs and QWLs. From Figs. 21 and 22 we can deduce that this typically happens only near the threshold injection , also we see that both of polarization and amplitude modulation response function increase by increasing $\frac{J}{J_T}$ nonlinearly . Note that increasing τ_c does not have much effect on ω_R^{PM} and ω_R^{AM}. The discontinuity of ω_{Peak} for the QDL is due to low-frequency roll-off. Due to the interaction of $\acute{\tau}_c$ and $\acute{\omega}_r$, shown in Eq. (25), $\omega_{Peak} = 0$ [40] only above injection $J_0 \sim 5/7J_T$.

In the previous sections, we created an analogy between stationary state and dynamical operation, showing that notable differences emerge in the analysis of small signals due to the associated variation in ϵ. We now consider if these differences related to the selection of ϵ_s and ϵ_d remain in the stationary state scenario.

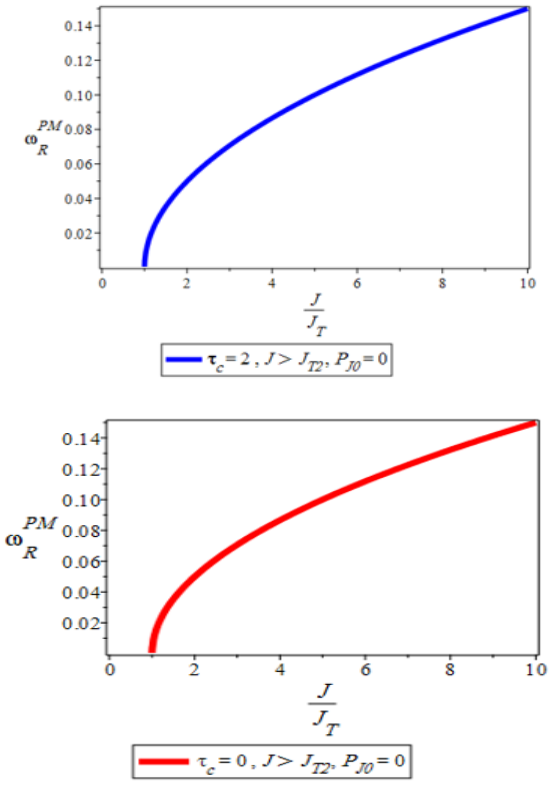

Figure 21. variations of polarization modulation response function in terms of $\frac{J}{J_T}$ in the states $J > J_{T2}, \tau_c = 0 \; and \; 2$

In Fig. 14, we examine the features of light injection and the density of carrier injection. The light intensity at $J = 10J_T$ for the QWL dynamical analogy (ϵ_d) is roughly 10% higher than that for QDLs and QWLs steady state analogy (ϵ_s).

5. Steady state versus dynamical operation gain compression

The acknowledgment of the connection between the increasing capture time in QDLs and the escalating gain compression coefficient in QWLs established the basis for both the stationary state and dynamical analogy. In the previous graphs, (refer to Fig. 14), we focused on a capture duration ($\tau_c = 2ps$).

In Fig. 20, we plotted the ϵ_s and ϵ_d in terms of the capture time of QDLs, which is correlated with QWLs, across various gain coefficients. These findings indicate that upon examining the two analogies, ϵ_s consistently whereas a reduction in gain continues at its rate. Consequently, ϵ_d must stop increasing and even begin to decline with $\tau_c$to offset the rapidly diminishing gain, resulting in the highest ϵ_d in Fig. 19.

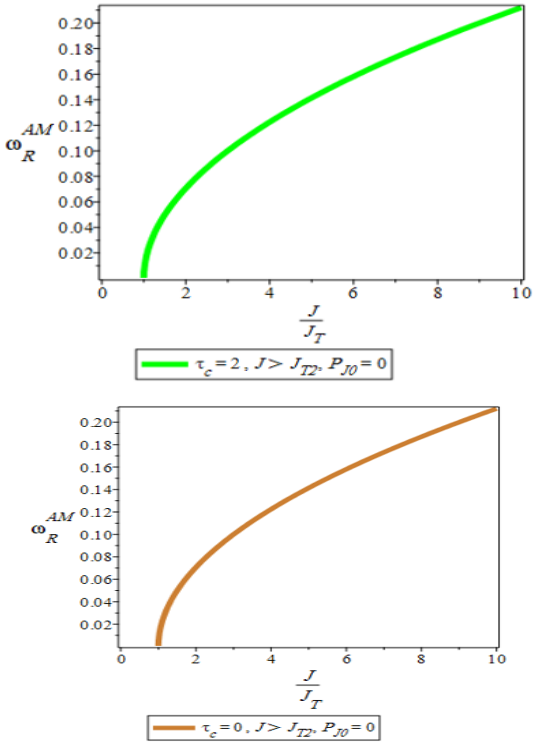

Figure 22. variations of amplitude modulation response function in term of $\frac{J}{J_T}$ in the states $J > J_{T2}$, $\tau_c = 0$ *and* 2, $P_{J0} = 0$

This surprising behavior of ϵ_d indicates a rapid decrease in decrease of the correlated QWL gaing_0. The highest bandwidth ω_{3dB}^{max} of a QDL decreases with growing τ_c, and in keeping the equal value of ω_{3dB}^{max} in QWL rate equations, $\epsilon_d$and g_0 are critically important. As τ_c rises, , g_0 decreases and B increases in line with the conditions (2) and (3) mentioned previously. After τ_c~$30ps$, ω_{3dB}^{max} starts to stabilize at $2Bn_T$, whereas a reduction in gain continues at its rate. Consequently, ϵ_d must stop increasing and even begin to decline with $\tau_c$to offset the rapidly diminishing gain, resulting in the highest ϵ_d in Fig. 19.

6. Analogy of spin lasers

surpassesϵ_d, leading to an oversuppression of dynamical response when the stationary-state analogy of QDLs is utilized. Although $\epsilon_s$shows a shows an increase with τ_c. Specifically, ϵ_d reaches a local maximum at τ_c~$30\ ps$ for $g\tau_{Ph} = 2$ and begins to decline for larger τ_c. This surprising behavior of ϵ_d indicates a rapid decrease in decrease of the correlated QWL gaing_0. The highest bandwidth ω_{3dB}^{max} of a QDL decreases with growing τ_c, and in keeping the equal value of ω_{3dB}^{max} in QWL rate equations, $\epsilon_d$and g_0 are critically important. As τ_c rises, , g_0 decreases and B increases in line with the conditions (2) and (3) mentioned previously. After τ_c~$30ps$, ω_{3dB}^{max} starts to stabilize at $2Bn_T$,

The experimental realization of spin-lasers [36]-[41] presents two important opportunities. The lasers provide a path to practical room-temperature spintronic devices with different operating principles, not limited to magnetoresistive effects, which have enabled tremendous advances in magnetically stored information [42]-[47]. This requires revisiting the common understanding of material parameters for desirable operation, as well as a departure from more widely studied unipolar spintronic devices, where only one type of carrier (electrons) plays an active role. In contrast, since semiconductor lasers are bipolar devices, a simultaneous description of electrons and holes is crucial. On the other hand, the interest in spin-lasers is not limited to spintronics, as they could extend the limits of what is feasible with conventional semiconductor lasers. At room temperature an order of magnitude faster operation than best conventional lasers was demonstrated in spin-lasers [46], while simultaneously supporting an order of magnitude lower-power consumption. This could enable future high-performance interconnects, which is particularly important since the dominant power consumption is increasingly determined by interconnects and information transfer rather than by transistors and information processing [6]-[8].

Theoretical studies of spin-lasers mostly focus only on spin-polarized electrons, the holes are merely spectators with vanishingly short spin relaxation time, losing their spin polarization instantaneously. Even simple questions remain topics of current research. Is longer spin relaxation always better? How does a simultaneous spin relaxation of electrons and holes affect the operation? Could spin-lasers inspire other device concepts in spintronics?

Previous analysis of correlates was restricted to the scenario where injected spin polarized is not present ($P_j = 0$). The wider case of spin lasers ($P_j \neq 0$) adds more complexity to the rate equations, requiring a number of 4 equations for QWLs and 10 for QDLs. For quantum dots, this added complexity obstructs analytical solutions even in a steady state, making it harder to directly apply the analogy for spin lasers. In addition, this complexity implies that the ability to explore QD spin lasers using a more straightforward description for QW spin lasers will be more meaningful than in classical lasers. Additionally, significant recent studies on

quantum dot-based spin lasers [31],[32] are described through the QW spin laser rate equations, and it is not clear how accurate this approach. These spin lasers are executed in a Faraday configuration [33],[34] as vertical cavity surface emitting lasers [45],[46]. The main distinction from commercially available vertical cavity surface emitting lasers is the generation of spin polarized carriers, which are introduced using circularly polarized light for pumping or by utilizing magnetic links for electrical spin injection [37],[38].

In spin lasers, we examine spin-resolved metrics to depict various helicities of light or spin projections. The total density of holes or electrons can be represented as the sum of the upward spin (+) and downward spin (−) densities, with $n = n_- + n_+$ and $p = p_- + p_+$. In the same way, we denote the overall density of the photon as the sum of the negative (−) and positive (+) helicities $s = s^- + s^+$An extension of the optical gain factor in Eq. (6) for QW spin lasers can be represented as

$$g_\pm(n_\pm, S^\pm) = g_0(n_\pm + p_\pm - n_{tran}) \Big/ \left(1 + \epsilon_+^\pm S^+ + \epsilon_-^\pm S^-\right) \quad (27)$$

Where $g_\pm$ denotes the gain of spin-dependent linked to the particular carrier's spin $n_\pm$. The ϵ superscript signifies the related carriers spin, while the subscript shows the associated photon's helicity. Because of symmetry, $\epsilon_+^- = \epsilon_-^+ = \epsilon_{cross}$, and $\epsilon_+^+ = \epsilon_-^- = \epsilon_{self}$. The index self (cross) signifies a self-(cross-) compression gain system. Subsequently, here (Fig. 20), we contrast the limit of self-compression ($\epsilon_{self} = 2\epsilon$, $\epsilon_{cross} = 0$) with the limit of even-compression ($\epsilon_{self} = \epsilon_{cross} = \epsilon$). Each scenario obtains the rate equations of a laser with spin unpolarized($P_J = 0$). To consider a link between QD spin lasers and QW spin lasers, we revisit our mapping method previously mentioned for $P_J = 0$.

We work on the regime with notable spin asymmetry of the hole-electron, which has been shown to lead to optimal threshold reduction and advantageous dynamical characteristics of spin lasers, where the time of spin relaxation for electrons is notably greater than that for holes. In spin lasers, it is hence common to investigate that holes are spin unpolarized. For simplicity, we mainly focus on the premise of infinitely long time spin relaxation for electrons (in wetting layer, QD, and QW zones). This restrictive situation can accurately depict recent experiments [45],[46] ,in which the time of spin relaxation for holes is not only much shorter than that for electrons but also significantly exceeds the other pertinent timescales for the carriers. The injection of light properties obtained for the anology of QD spin lasers to QW spin lasers with self-compression are depicted in Fig. 14.

Several important aspects of spin lasers that can already be deduced from the bucket model in Fig. 2(b) are evidently present .With $P_J \neq 0$ the thresholds for majority and minority spin (J_{T_1},J_{T_2}) are different. Since $\left(J_{T_1} < J_T < J_{T_2}\right)$there is a threshold reduction (recall Eq. (2)), as compared to classical lasers. Furthermore, for injection $\left(J_{T_1} < J_T < J_{T_2}\right)$ there will be a spin-filtering effect Eq. (3); even a modest injection leads to fully polarized emitted light [41]. Even though our results have been based on parameters identical to the ones used for classical lasers (supplemented by the vanishing hole and infinite electron spin relaxation times).

We uphold a robust connection between QDLs and QWLs, especially near the two thresholds. For instance, in Fig. 14 concerning the dynamical analogy characterized by ε_d, the emitted right CP, s^+, is almost identical between the QDLs and QWLs. We additionally consider the analogy of spin lasers in Fig. 20; the inset depicts the variation of minority and majority thresholds with injection polarization, for both self and even-compression of gain. There is significant consensus on J_{T_1} for all P_J's and a satisfactory correlation of J_{T_2} up to P_J~0.6, signifying that, within the practical injection polarization of spin lasers achieved at room temperature, the proposed analogy operates successfully.

From the correlation of J_{T_2} on P_J in QDLs, we observe that their performance is situated between that of the quantum well approximations employing even and self compression. The identical pattern, i.e., J_{T_2} of a quantum dot limited by the two extreme scenarios for the gain compression of QWLs, is depicted in the primary panel as in terms of τ_c with constantP_J. The J_{T_2} in QWLs vanishes for even compression approximation, which can be observed in the inset ($P_J \approx 0.83$) and within the primary panel ($\tau_c \approx 10ps$). On the other hand, J_{T_2}does not vanish for QWL. The notable precision of the J_{T_1} analogy is not restricted to the particular assumption of compression gain and remains valid over a broad spectrum of parameters. As a result, the decrease in the threshold Eq. (2) of QDLs is precisely illustrated through an analogy to QWLs.

The spin-filtering condition, outlined by Eq. (3) is revealed in both QDLs and QWLs; however, its variance on J_{T_2}indicates low accuracy with high amounts ofτ_c andP_J, while the latter parameter range holds less importance in experiments. It is essential to highlight that in Fig. 20, only ϵ_s is employed for the computation, as the results remain unchanged by the difference betweenϵ_d and ϵ_s . The change in J_{T_2} due to the disparity between ϵ_d and $\epsilon_s$is less than 2%.

7. Analysis of the small signal for spin lasers

Fueled by the preliminary stationary state evaluations on spin lasers, it was expected that the identified threshold decrease could result in better dynamical performance and enhanced bandwidth [39]-[41]. Recent advancements in electrical and injection of optical spin [40]-[45] provide options for spin lasers modulation. In previous works, QW spin lasers, with amplitude and polarization modulation were investigated [42]. Amplitude modulation for a stationary state polarization suggests $J_+ \neq J_-$:

$$J = J_0 + Re[\delta J(\omega)e^{-i\omega t}], \quad P_J = P_{J_0} \quad (28)$$

As observed in the stationary state evaluation, $P_J \neq 0$ leads to varying J_{T_1} and J_{T_2}, which is clearly shown in the bucket method depicted in Fig. 2(b). This category of modulation can be likened to polarization modulation, in which$J_+ \neq J_-$, but J do not change [46]:

$$P_J = P_{J_0} + \mathrm{Re}\left[\delta P_J(\omega)e^{-i\omega t}, J = J_0\right] \quad (29)$$

It was recently demonstrated that a comparable polarization modulation method could facilitate high operation spin communication systems with an effective data transfer rate that surpasses existing implementations by several orders of magnitude . We extend the analysis of small signal described in Section choice of the gain compression coefficient ϵ in the simple form of QWLs. However, the way in which τ_c should connect to ϵ remains uncertain; we notice considerable differences between the correlate of stationary state and dynamical operations of lasers, corresponding to the respective gain compression coefficients ϵ_d and ϵ_s .The stationary state analogy effectively represents the character of a QDL as it nears its threshold, relevant for both classical lasers and spin lasers. In the context of spin lasers, for any given spin polarized laser, the majority threshold is notably accurate, further supporting the use of QW spin laser rate equations for reducing thresholds [33]. Both spin-lasers and their conventional counterparts share three main elements: (i) the active (gain) region, responsible for optical amplification and stimulated emission, (ii) the resonant cavity, and (iii) the pump, which injects (optically or electrically) energy/carriers. The main distinction of spin-lasers is the net carrier spin polarization (spin imbalance) in the active region, which leads to crucial changes in their operation.Most of the spin-lasers are implemented as vertical-cavity surface-emitting lasers (VCSELs) [4] with the gain region based on quantum wells (QWs) or quantum dots (QDs), adding to their conventional counterparts electrically or optically injected spin-polarized carriers. There are three major differences between spin-lasers and their conventional counterparts. (i) Injected carriers are spin polarized. (ii) The light emitted is circularly polarized due to the spin-polarized carriers. When an electron recombines with a hole in accordance with optical selection rules, the electron spin orientation determines the helicity (circular polarization) of the emitted photon, such that the total angular momentum is conserved. In examining the dynamical range analogy, we notice on the preserving the highest bandwidth of both QDLs and QWLs, since their complex character can illustrate notable distinctions, like roll-off low frequency in the response of modulation [39]. Another reason for this method is that the injection level impacts the bandwidth itself, rendering it a less favorable parameter for alignment in the analogy. The rising interest in QDLs and the expanding range of materials used for the active region [30]–[33] .As the analogy is not restricted to classical lasers, it can also be applied to help future developments in QD spin lasers. The presence of quantum dots in the active zone leads to decreased L-S 4 and compare our findings for classical lasers with those for spin lasers, employing self compression and ϵ_d . The response function can be expressed as: $R_{\pm}(\omega) = \left|\delta S^{\mp}(\omega)/\delta J_{\pm}(\omega)\right|$ for spin lasers, and it simplifies $R(\omega)$.

8. Conclusion

We have created a systematic method that enables the correlation between QDLs and QWLs, therefore, streamlining the explanation of QDLs through rate equations. The fundamental understanding for creating this analogy is that the influence of finite τ_c on QDLs operations can be accurately represented by a proper coupling effects [26], which prolongs the time of spin relaxation, improving lasing characteristics and consequently lowering the threshold and expanding bandwidth. A thorough comprehension of the frameworks employed in recent research on QD spin lasers [21] would allow us to use the previously mentioned analogy and investigate its relationship to a characterization based on densities rather than occupancies [22]. Certain aspects of the existing analogy could be loosened. To enable a broader RE representation of QDLs, it might be possible to explicitly include a finite gain compression coefficient in QDL rate equations . The expected change in the analogy process will involve a suitably higher ϵ for QWLs, fulfilling both the role of the ϵ of the QDLs and the limited τ_c. Through additional research into even and self compression processes, it would be possible to model gain compression more precisely, incorporating appropriately balanced contributions from both mechanisms (as indicated by the matrix format of $\varepsilon_{\pm}^{\pm}$). Future developments of the analogy process may also consider the time of spin relaxation of holes. While the holes spin in bulk GaAs at room temperature can be regarded as lost almost instantaneously [24], in quantum dots, the difference in time of spin relaxation between holes and electrons is anticipated to be decreased [26]. In future studies, it would be fascinating to investigate different types of mapping methods that might reveal similarities between phase transitions and spin lasers in magnetic devices. Such analysis would expand the current knowledge regarding classical lasers, particularly those related to lasing ferromagnets [44],[45], and clarify how the spin imbalance native to spin lasers can be connected to more complex magnetic phenomena through appropriate steady states. Future research on quantum dot (QD) and quantum well (QW) spin-polarized lasers should focus on improving spin injection efficiency and stability under electrical operation at room temperature, optimizing heterostructure design to enhance spin lifetime and reduce spin relaxation, and developing accurate kinetic models linking carrier spin dynamics to lasing performance. Comparative studies between QD and QW active regions can clarify how quantum confinement affects polarization control, threshold reduction, and modulation speed. Exploring new materials such as GeSn alloys, perovskites, and colloidal QDs could

further enhance spin coherence and wavelength tunability. Additionally, integrating spin lasers with photonic circuits for polarization-encoded data transmission and investigating ultrafast polarization modulation, bistability, and quantum information applications represent promising directions for advancing spintronic photonics.

Authors Contribution
All authors conceived of the study, participated in its design and coordination, drafted the manuscript, participated in the sequence alignment, and read and approved the final manuscript.

Availability of data and materials
Not applicable. In fact, all results are obtained without any software and found by manual computations. In other words, the manuscript is in the pure mathematics (mathematical analysis) category.

Conflict of interests
The author states that there is no conflict of interest.

References

[1] A. Hohl and A. Gavrielides, "Bifurcation cascade in a semiconductor laser subject to optical feedback," Phys. Rev. Lett., vol. 82, pp. 1148–1151, 1999, doi: 10.1103/PhysRevLett.82.1148

[2] M. C. Soriano, J. Garcia-Ojalvo, R. Mirasso, et al., "Complex photonics: dynamics and applications of delay-coupled semiconductor lasers," Rev. Mod. Phys., vol. 85, pp. 421–470, 2013, doi: 10.1103/RevModPhys.85.421

[3] J. J. Chen, Y. N. Duan, L. F. Li, et al., "Wideband polarization-resolved chaos with time-delay signature suppression in VCSELs subject to dual chaotic optical injections," IEEE Access, vol. 6, pp. 66807–66815, 2018, doi: 10.1109/ACCESS.2018.2878734

[4] F. Y. Lin and J. M. Liu, "Nonlinear dynamics of a semiconductor laser with delayed negative optoelectronic feedback," IEEE J. Quantum Electron., vol. 39, pp. 562–568, 2003, doi:10.1109/JQE.2003.809338

[5] P. Guo, W. Yang, D. Parekh, et al., "Experimental and theoretical study of wide hysteresis cycles in 1550 nm VCSELs under optical injection," Opt. Express, vol. 21, pp. 3125–3132, 2013, doi: 10.1364/OE.21.003125

[6] [6] T. Wang, Y. D. Yang, Y. Z. Hao, et al., "Nonlinear dynamics of a semiconductor microcavity laser subject to frequency comb injection," Opt. Express, vol. 30, pp. 45459–45470, 2022, doi: 10.1364/OE.475651

[7] Z. W. Xu, H. Tian, Z. Zeng, et al., "Time-delay signature suppression of the chaotic signal in a semiconductor laser based on optoelectronic hybrid feedback," Opt. Express, vol. 31, pp. 39454–39464, 2023, doi: 10.1364/OE.504489

[8] Y. Huang, P. Zhou, Y. Zeng, et al., "Evolution of extreme events in a semiconductor laser subject to chaotic optical injection," Phys. Rev. A, vol. 105, Art. no. 043521, 2022, doi: 10.1103/PhysRevA.105.043521

[9] L. Y. Zhang, W. Pan, L. S. Yan, et al., "Independently synchronizable groups in networks of delay-coupled semiconductor lasers," IEEE J. Sel. Top. Quantum Electron., vol. 28, pp. 1–6, 2022, doi: 10.1109/JSTQE.2021.3091901

[10] Y. Kawaguchi, T. Okuma, K. Kanno, et al., "Entropy rate of chaos in an optically injected semiconductor laser for physical random number generation," Opt. Express, vol. 29, pp. 2442–2457, 2021, doi: 10.1364/OE.411694

[11] A. M. Sciamann and K. A. Shore, "Physics and applications of laser diode chaos," Nat. Photonics, vol. 9, pp. 151–162, 2015, doi: 10.1038/nphoton.2014.326

[12] B. C. Liu, Y. Y. Xie, Y. Z. Liu, et al., "A novel double masking scheme for enhancing security of optical chaotic communication based on two groups of mutually asynchronous VCSELs," Opt. Laser Technol., vol. 107, pp. 122–130, 2018, doi: 10.1016/j.optlastec.2018.05.022

[13] A. Uchida, K. Amano, M. Inoue, et al., "Fast physical random bit generation with chaotic semiconductor lasers," Nat. Photonics, vol. 2, pp. 728–732, 2008, doi: 10.1038/nphoton.2008.227

[14] G. Tanaka, T. Yamane, J. B. Héroux, et al., "Recent advances in physical reservoir computing: a review," Neural Netw., vol. 115, pp. 100–123, 2019, doi: 10.1016/j.neunet.2019.03.005

[15] Y. H. Hung and S. K. Hwang, "Photonic microwave amplification for radio-over-fiber links using period-one nonlinear dynamics of semiconductor lasers," Opt. Lett., vol. 38, pp. 3355–3358, 2013, doi: 10.1364/OL.38.003355

[16] H. Liu, T. Wang, Q. Jiang, et al., "Long-wavelength InAs/GaAs quantum-dot laser diode monolithically grown on Ge substrate," Nat. Photonics, vol. 5, pp. 416–419, 2011, doi: 10.1038/nphoton.2011.120

[17] S. Chen, W. Li, J. Wu, et al., "Electrically pumped continuous-wave III–V quantum dot lasers on silicon," Nat. Photonics, vol. 10, pp. 207–312, 2016, doi: 10.1038/nphoton.2016.21

[18] D. Jung, Z. Zhang, J. Norman, et al., "Highly reliable low-threshold InAs quantum dot lasers on on-axis (001) Si with 87% injection efficiency," ACS Photonics, vol. 5, pp. 1094–1100, 2018, doi: 10.1021/acsphotonics.7b01387

[19] J. C. Norman, D. Jung, Z. Zhang, et al., "A review of high-performance quantum dot lasers on silicon," IEEE J. Quantum Electron., vol. 55, Art. no. 2000511, 2019, doi: 10.1109/JQE.2019.2901508

[20] A. Malik, J. Guo, M. A. Tran, et al., "Widely tunable, heterogeneously integrated quantum-dot O-band lasers on silicon," Photon. Res., vol. 8, pp. 1551–1557, 2020,

doi: 10.1364/PRJ.394726

[21] Y. Wan, J. C. Norman, Y. Tong, et al., "1.3 μm quantum dot-distributed feedback lasers directly grown on (001) Si," Laser Photon. Rev., vol. 14, Art. no. 2000037, 2020, doi: 10.1002/lpor.202000037

[22] A. Capua, L. Rozenfeld, V. Mikhelashvili, et al., "Direct correlation between a highly damped modulation response and ultralow relative intensity noise in an InAs/GaAs quantum dot laser," Opt. Express, vol. 15, pp. 5388–5393, 2007, doi: 10.1364/OE.15.005388

[23] A. Y. Liu, T. Komljenovic, M. L. Davenport, et al., "Reflection sensitivity of 1.3 μm quantum dot lasers epitaxially grown on silicon," Opt. Express, vol. 25, pp. doi: 10.1039/C8NR05677C

[26] H. Irie, T. Akiho, and K. Muraki, "Determination of g - factor in InAs two-dimensional electron system by capacitance spectroscopy," *Appl. Phys. Express*, vol. 12, no. 6, p. 063004, Jun. 2019, doi: 10.7567/1882-0786/ab1c7c

[27] L. Olejniczak, K. Panajotov, S. Wieczorek, et al., "Intrinsic gain switching in optically injected quantum dot laser lasing simultaneously from the ground and excited state," J. Opt. Soc. Am. B, vol. 27, pp. 2416–2423, 2010, doi: 10.1364/JOSAB.27.002416

[28] F. Grillot, J. C. Norman, J. Duan, et al., "Physics and applications of quantum dot lasers for silicon photonics," Nanophotonics, vol. 9, pp. 1271–1286, 2020, doi: 10.1515/nanoph-2019-0570

[29] D. Goulding, S. P. Hegarty, O. Rasskazov, et al., "Excitability in a quantum dot semiconductor laser with optical injection," Phys. Rev. Lett., vol. 98, Art. no. 153903, 2007, doi: 10.1103/PhysRevLett.98.153903

[30] M. Dillane, B. Tykalewicz, D. Goulding, et al., "Square wave excitability in quantum dot lasers under optical injection," Opt. Lett., vol. 44, pp. 347–350, 2019, doi: 10.1364/OL.44.000347

[31] L. C. Lin, C. Y. Chen, H. Huang, et al., "Comparison of optical feedback dynamics of InAs/GaAs quantum-dot lasers emitting solely on ground or excited states," Opt. Lett., vol. 43, pp. 210–213, 2018, doi: 10.1364/OL.43.000210

[32] H. Lin, Y. H. Hong, S. Ourari, et al., "Quantum dot lasers subject to polarization-rotated optical feedback," IEEE J. Quantum Electron., vol. 56, Art. no. 2000308, 2020, doi: 10.1109/JQE.2019.2953518

[33] D. Arsenijević, A. Schliwa, H. Schmeckebier, et al., "Comparison of dynamic properties of ground- and excited-state emission in p-doped InAs/GaAs quantum-dot lasers," Appl. Phys. Lett., vol. 104, Art. no. 181101, 2014, doi: 10.1063/1.4875238

9535–9543, 2017, doi: 10.1364/OE.25.009535
O. B. Shchekin and D. G. Deppe, "1.3 μm InAs quantum dot laser with T0 = 161 K from 0 to 80°C," Appl. Phys. Lett., vol. 80, pp. 3277–3279, 2002, doi: 10.1063/1.1476708

[24] R. L. Sellin, C. Ribbat, M. Grundmann, et al., "Close-to-ideal device characteristics of high-power InGaAs/GaAs quantum dot lasers," Appl. Phys. Lett., vol. 78, pp. 1207–1209, 2001, doi: 10.1063/1.1350596

[25] C.T. Chou, N. T. Jacobson, *et al.*, "Weak anti-localization of two-dimensional holes in germanium beyond the diffusive regime," *Nanoscale*, vol. 10, no. 44, pp. 20559–20564, 2018,

[34] C. Wang, B. Lingnau, K. Lüdge, et al., "Enhanced dynamic performance of quantum dot semiconductor lasers operating on the excited state," IEEE J. Quantum Electron., vol. 50, pp. 723–731, 2014, doi: 10.1109/JQE.2014.2361480

[35] M. Virte, S. Breuer, M. Sciamanna, et al., "Switching between ground and excited states by optical feedback in a quantum dot laser diode," Appl. Phys. Lett., vol. 105, Art. no. 121109, 2014, doi: 10.1063/1.4896576

[36] M. Virte, K. Panajotov, M. Sciamanna, "Mode competition induced by optical feedback in two-color quantum dot lasers," IEEE J. Quantum Electron., vol. 49, pp. 578–585, 2013, doi: 10.1109/JQE.2013.2260725

[37] B. Tykalewicz, D. Goulding, S. P. Hegarty, et al., "All-optical switching with a dual-state, single-section quantum dot laser via optical injection," Opt. Lett., vol. 39, pp. 4607–4609, 2014, doi: 10.1364/OL.39.004607

[38] B. Kelleher, B. Tykalewicz, D. Goulding, et al., "Two-color bursting oscillations," Sci. Rep., vol. 7, Art. no. 8414, 2017, doi:10.1038/s41598-017-08751-y

[39] B. Tykalewicz, D. Goulding, S. P. Hegarty, et al., "Optically induced hysteresis in a two-state quantum dot laser," Opt. Lett., vol. 41, pp. 1034–1037, 2016, doi: 10.1364/OL.41.001034

[40] S. Meinecke, B. Lingnau, A. Röhm, et al., "Stability of optically injected two-state quantum-dot lasers," Ann. Phys., vol. 529, Art. no. 1600279, 2017, doi: 10.1002/andp.201600279

[41] E. A. Viktorov, P. Mandel, I. O'Driscoll, et al., "Low-frequency fluctuations in two-state quantum dot lasers," Opt. Lett., vol. 31, pp. 2302–2304, 2006, doi: 10.1364/OL.31.002302

[42] E. A. Viktorov, I. Dubinkin, N. Fedorov, et al., "Injection-induced, tunable, all-optical gating in a two-state quantum dot laser," Opt. Lett., vol. 41, pp. 3555–3558, 2016, doi: 10.1364/OL.41.003555

[43] A. Dehghaninejad, M. M. Sheikhey, H. Baghban, "Dynamic behavior of injection-locked two-state quantum dot lasers," J. Opt. Soc. Am. B, vol. 36, pp. 1518–1524, 2019, doi: 10.1364/JOSAB.36.001518

[44] C. Wang, J. P. Zhuang, F. Grillot, et al., "Contribution of off-resonant states to the phase noise of quantum dot lasers," Opt. Express, vol. 24, pp. 29872–29880, 2016, doi: 10.1364/OE.24.029872

[45] F. Grillot, C. Wang, N. A. Naderi, et al., "Modulation properties of self-injected quantum-dot semiconductor diode lasers," IEEE J. Sel. Top. Quantum Electron., vol. 19, Art. no. 1900812, 2013, doi: 10.1109/JSTQE.2013.2246776

[46] Z. F. Jiang, Z. M. Wu, E. Jayaprasath, W. Y. Yang, et al., "Nonlinear dynamics of exclusive excited-state emission quantum dot lasers under optical injection," Photonics, vol. 6, Art. no. 58, 2019, doi: 10.3390/photonics6020058